Materials Advances

PAPER

View Article Online
View Journal | View Issue

Cite this: *Mater. Adv.*, 2025, **6**, 827

Ultra-high-sensitive temperature sensing based on emission Pr^{3+} and Yb^{3+} codoped $Y_2Mo_3O_{12}$ nanostructures†

Nozha Ben Amar,[a] Kamel Saidi,*[ab] Christian Hernández-Álvarez,[b] Mohamed Dammak*[a] and Inocencio R. Martin[b]

Received 24th July 2024,
Accepted 9th December 2024

DOI: 10.1039/d4ma00746h

rsc.li/materials-advances

In recent years, non-contact fluorescence intensity ratio (FIR)-based luminescent thermometry has garnered significant attention for its potential applications in various fields, including electromagnetic environments, micro-temperature fields, and thermally harsh conditions. In this study, we focus on the synthesis and characterization of $Y_2Mo_3O_{12}$ co-doped with 2% Pr^{3+} and 15% Yb^{3+} nanoparticles using a sol–gel reaction method. The phase purity and luminescence characteristics of the synthesized nanoparticles were thoroughly evaluated using techniques such as X-ray diffraction (XRD), scanning electron microscopy (SEM), and photoluminescence (PL). Upon excitation with 457 nm light, intense emissions from the $^3P_0$, $^3P_1$ and $^1D_2$ excited states were observed. The temperature sensing capabilities of the nanoparticles were investigated within the range of 298–448 K. Furthermore, the thermal and non-thermal coupling levels of Pr^{3+} and Yb^{3+} ions were analysed using fluorescence intensity ratio technique (FIR). Our results demonstrated that $Y_2Mo_3O_{12}$ co-doped with 2% Pr^{3+} and 15% Yb^{3+} exhibited high sensitivity in temperature sensing, with a maximum relative sensitivity of 11.2% K^{-1} observed at 298 K. Notably, temperature uncertainty (δT) values were exceptionally low within the range of 0.11–0.63 K. These findings underscore the potential of $Y_2Mo_3O_{12}$:Pr^{3+}/Yb^{3+} nanoparticles in optical thermometry applications, thus highlighting their effectiveness as temperature sensors in various environments.

I. Introduction

Temperature is a crucial physical parameter in several domains, including scientific study, engineering, and mechanical production. Non-contact optical temperature systems using luminous materials have addressed the limitations of conventional contact thermometers and have been widely researched and used.[1–3] Luminescence thermometry enables estimating the local temperature of an item with sub-micrometric spatial resolution, which is very significant for basic biology, medicine, and industry. The determination of temperature may be achieved by detecting and evaluating a temperature-dependent luminescence signal.[4–7] Submicrometric spatial resolution may be accomplished by employing particular nanosized materials that function in an ultraviolet, visible and/or near-infrared spectral range. The sensors working in the physiological temperature range are highly essential for hypothermia testing[8] and thermometry of live cells.[9] Sensors working at higher temperatures are effective in the temperature mapping of microcircuits, as per studies reported over the last few decades, and numerous luminous materials (*e.g.*, organic dyes, polymers, quantum dots, and rare-earth-based materials) have been explored based on the temperature-dependent connection between fluorescence intensity and temperature.[10–13] Among them, lanthanide-based (Ln^{3+}-based) inorganic up-conversion and down-conversion materials have drawn much more research interest on account of abundant ion species (such as Er^{3+}, Tm^{3+}, Nd^{3+}, Pr^{3+}, Tb^{3+}, and Eu^{3+} ions). More high-performance detection methods can be developed, allowing temperature readings to become more varied.[14–17] Additionally, trivalent praseodymium (Pr^{3+}) is a desirable option among activator rare-earth (RE) ions owing to its fluorescence across visible, ultraviolet, and near-infrared wavelengths. Interestingly, it produces red and green-blue light, originating from transitions in the $^1D_2$ and $^3P_0$ multiplets, respectively.[18,19] Pr^{3+}-doped phosphors have demonstrated promising sensing properties.[20–22] Trivalent ytterbium (Yb^{3+}) ions are frequently used as sensitizers because of to the $^2F_{7/2} \rightarrow {}^2F_{5/2}$ transition, which exhibits a high absorption cross-section for 980 nm near-infrared light. This makes energy transfer from Yb^{3+} to Pr^{3+} highly efficient.[23,24] Particularly notable

---

[a] *Laboratoire de Physique Appliquée, Faculté des Sciences de Sfax, Département de Physique, Université de Sfax, BP 1171, Université de Sfax, 3018 Sfax, Tunisie. E-mail: madidammak@yahoo.fr, saidikamel494@gmail.com*

[b] *Departamento de Física, Instituto Universitario de Materiales y Nanotecnología (IMN), Universidad de La Laguna, San Cristóbal de La Laguna E38200, Spain*

† Electronic supplementary information (ESI) available. See DOI: https://doi.org/10.1039/d4ma00746h

is the synergistic combination of praseodymium (Pr^{3+}) and ytterbium (Yb^{3+}), which, under 980 nm infrared excitation, enhances the thermometric performance, thereby extending the applicability of luminescent thermometry to previously inaccessible environments. The optical thermometric behavior of Pr^{3+}/Yb^{3+} has been studied in several compounds based on upconversion emission spectra.[25,26] Nowadays along with the increasingly stringent temperature sensing demands of industrial production and scientific research, the development of new temperature sensing strategies is important for improving the capability of luminescent thermometers and satisfying the application requirements of micro- or nano-functional devices. Numerous optical sensing devices using lanthanide ion-doped materials for thermometric properties have been documented.[27–29] One of the key tactics in optical temperature sensing presently being developed is the fluorescence intensity ratio (FIR) technology.[30–32] This method helps to eliminate the impact of external factors such as changes in geometry, excitation source power, and light field. FIR technology typically needs two thermally associated energy levels (TCLs) of lanthanide ions or non-thermally coupled energy levels (NTCLs) with dual or multiple centres. TCL-based optical thermometry has limited sensitivity and temperature range owing to a small energy gap and spectral overlap, making it unsuitable for practical applications.[33,34] Using NTCLs for optical thermometry can be problematic due to measurement interference. The relative luminescence intensities of different luminescent centres vary with excitation wavelength and power, making reliability a concern.[35] Finding appropriate luminescent materials for temperature sensors employing FIR technology is crucial for achieving high sensitivity and working over a broad temperature range. Crucial to the usefulness of lanthanide-based thermal sensors is the selection of an appropriate host material, which dramatically effects their performance and stability. Molybdates occupy enormous relevance as inorganic compounds, displaying excellent performance in catalysis, laser technology, and as ionic conductors.[36–39] A recent study has significantly dived into examining the luminescence characteristics of molybdates doped with rare earth ions.[16,40,41] It is worth mentioning that the optical characteristics of molybdates are very structure-dependent and they may exist in distinct crystal phases with varying valences of molybdenum element. Molybdate hosts have emerged as frontrunners, displaying outstanding thermal stability and compatibility with lanthanide dopants. Inspired by this, the optical properties of 2% Pr^{3+}/15% Yb^{3+}-doped molybdate $Y_2Mo_4O_{15}$ hosts based on down-conversion emission have been studied in our previous work and the thermometric parameters were calculated.[42]

We selected $Y_2Mo_3O_{12}$ due to its remarkable properties, including the largest negative thermal expansion (NTE) and minimal anisotropy. These characteristics can be attributed to the large ionic radius and low electronegativity of yttrium (Y) atoms, which significantly influence the structural and thermal behavior of the material.[43,44] It presents many optical applications, especially when codoped with rare earth elements, such as $Y_2Mo_3O_{12}$ codoped Er^{3+}/Yb^{3+},[45–47] $Y_2Mo_3O_{12}:Tm^{3+}/Yb^{3+}$ (ref. 48) and $Y_2Mo_3O_{12}:Nd^{3+}/Yb^{3+}$.[49]

In this study, we investigate a novel luminescent material based on $Y_2Mo_3O_{12}$ co-doped with 2% Pr^{3+}/15% Yb^{3+} ions. By leveraging the luminescent properties of lanthanides within a molybdate host matrix, our research aims to advance the understanding of optical thermometry and pave the way for its widespread adoption across various industries and scientific disciplines. Through comprehensive analysis and characterization, we aim to elucidate the temperature-sensing capabilities of this material using the FIR technique ranging from 298 K to 448 K for both (TCLs) and (NTCLs) and its potential for real-world applications.

II. Experimental details

We synthesized Pr^{3+}/Yb^{3+} co-doped $Y_2Mo_3O_{12}$ using the sol–gel method. The primary reagents for sample preparation included $Y(NO_3)_3\cdot 6H_2O$ (99.8%), $Pr(NO_3)_3\cdot 5H_2O$ (99.9%), $Yb(NO_3)_3\cdot 5H_2O$ (99.9%), $(NH_4)_6Mo_7O_{24}\cdot 4H_2O$ (99%), and citric acid ($C_6H_8O_7$; 99.5%), all obtained from Sigma Aldrich. The required raw materials were weighed in stoichiometric amounts, dissolved in distilled water, and stirred magnetically at 80 °C for 1 hour to promote gel formation and eliminate excess water. The resulting xerogel was then placed in an oven at 120 °C for 12 hours. Following this step, the xerogels were transferred into alumina crucibles and calcined at 600 °C for 12 hours in a furnace.

III. Characterization techniques

The purity of the obtained compound was checked by X-ray diffraction (XRD) using a Bruker D8 diffractometer with Cu Kα radiation (λ_{cu} = 1.5418 Å) at room temperature. The sample's morphology was examined using scanning electron microscopy (SEM, FEI Quanta 250 FEG) equipped with an energy-dispersive X-ray spectroscopy (EDS) accessory. For temperature calibrations, the powder sample was placed in the centre of a tubular furnace, and the temperature was increased from room temperature (RT) to 448 K. A K-type thermocouple positioned near the sample, attached to a temperature calibrator (Fluke 714), provided precise temperature measurements. The fluorescence intensity ratio (FIR) approach is based on variations in the relative intensities between two bands of the emission spectrum. To obtain the emission spectra of the material, excitation was performed using a 457 nm continuous laser focused onto the sample. The luminescence from the sample was filtered using a short-pass filter, then focused at the tip of an optical fibre positioned on the opposite side of the furnace. The optical fibre was connected to a 0.3 m single grating spectrometer (Andor SR-3031-B), and the signal was measured using a cooled CCD detector (Newton DU920 N) with a resolution of 0.7 nm ($\sim$25 cm^{-1}) and an integration time of 1 s. Luminescence decay curves were recorded with a 200 MHz LeCroy WS424 oscilloscope, a photomultiplier tube (PMT)—Hamamatsu R928, and a tunable EKSPLA/NT342/3/UVE 10 ns pulsed laser (optical parametric oscillator—OPO) with a repetition rate of 10 Hz, which served as an excitation source.

IV. Results and discussion

1. Structural and morphological analysis

The powder X-ray diffraction profiles of $Y_2(MoO_4)_3$:2% Pr^{3+}/15% Yb^3 shown in Fig. S1 (ESI†) matched very well with the JCPDS#28-154. X-ray analysis shows that all diffraction peaks were in good agreement with the orthorhombic symmetry and space group *Pbcn*.[50] Using the XRD data, the structural parameters were refined by the Rietveld method, as shown in Fig. 1. The refinement results confirmed that the lattice parameters were a = 13.9419 Å; b = 9.7967 Å and c = 9.9561 Å, which are in agreement with the literature.[51] Taking into account the similar ionic radius $r(Pr^{3+})$ = 0.99 Å, $r(Y^{3+})$ = 0.9 Å and $r(Yb^{3+})$ = 0.985 Å, we suggest that the Pr^{3+} and Yb^{3+} ions are expected to most probably to occupy the Y^{3+} sites.[52]

The morphology of the $Y_2Mo_3O_{12}$:2% Pr^3/15% Yb^{3+} phosphor was carefully investigated using scanning electron microscopy (SEM) to evaluate the surface features and grain connectivity, as shown in Fig. 2a. The microstructure reveals a generally uniform distribution of grains, which shows a predominantly irregular shape. Some degree of agglomeration is visible, indicating potential interactions among particles during synthesis that could influence the sintering process. A detailed grain size distribution analysis is illustrated in Fig. 2b, showing a relatively narrow size range, which suggests a consistent particle formation mechanism throughout synthesis. The average grain size, calculated to be approximately 0.42 µm, implies a submicron scale that may favor high surface-to-volume ratios. This feature is often advantageous in optical materials as it can enhance light scattering and influence photoluminescent properties. The relatively small grain size might also contribute to improved thermal stability and homogeneous energy transfer between Pr^{3+} and Yb^{3+} ions within the matrix, potentially enhancing the upconversion efficiency.

Additionally, a close examination of the grain boundaries reveals that they are relatively well-defined, suggesting effective crystal growth and minimized grain boundary defects. This structural uniformity might reduce non-radiative losses, a beneficial factor for optical thermometry applications. Further, the submicron scale could support good dispersibility in polymer or solvent matrices if the material is intended for integration into nanocomposite systems for broader applications. To confirm the presence of all elements, the energy dispersive X-ray spectrum of $Y_2Mo_3O_{12}$:2% Pr^{3+}/15% Yb^{3+} is displayed in Fig. S2 (ESI†).

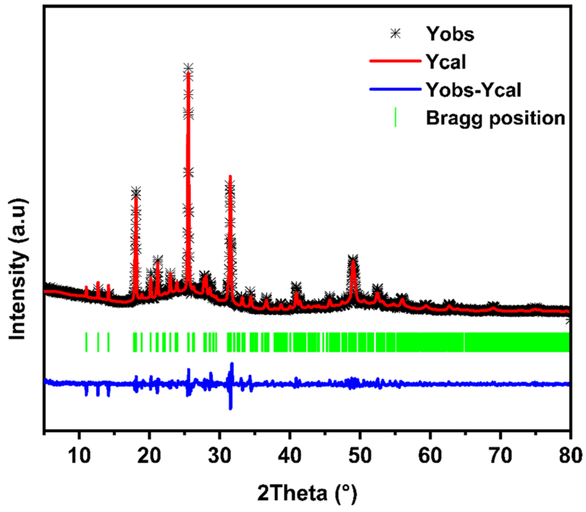

Fig. 1 XRD Rietveld refinement of $Y_2Mo_3O_{12}$:2% Pr^{3+}/15% Yb^{3+}.

The energy-dispersive X-ray spectra of $Y_2Mo_3O_{12}$ codoped Pr^{3+}/Yb^{3+} confirms the presence of the signals of (Y), (Mo), (O) and doped ions (Pr) and (Yb). No other impurity element is present in the EDX figure, which reveals the purity of the prepared sample and confirms the XRD analysis. The quantitative compositions are in good relation with nominal compositions of the $Y_2Mo_3O_{12}$:2% Pr^{3+}/15% Yb^{3+} particles. The sample contains Mo, Y, Yb, O and Pr elements, suggesting the successful formation of $Y_2Mo_3O_{12}$:2% Pr^{3+}/15% Yb^{3+} using the sol–gel method.

2. Photoluminescence properties of $Y_2Mo_3O_{12}$:Pr^{3+}/Yb^{3+}

Fig. 3a illustrates the photoluminescence spectrum of Pr^{3+}/Yb^{3+} in $Y_2Mo_3O_{12}$ at room temperature and is excited by 457 nm. Within the 510–1070 nm range, the observed photoluminescence arises from f–f transitions within Pr^{3+} originating from the $^3P_0$ and $^3P_1$ and $^1D_2$ states, as well as Yb^{3+} originating from the $^2F_{5/2}$ state. The observed emission were detected at 537 nm, 562 nm, 604 nm, 612 nm, 623 nm, 656 nm, 694 nm, 705 nm, 741 nm and 890 nm corresponding to transitions $^3P_1 \rightarrow {}^3H_5$, $^3P_0 \rightarrow {}^3H_5$, $^1D_2 \rightarrow {}^3H_4$,$^3P_0 \rightarrow {}^3H_6$, $^3P_1 \rightarrow {}^3F_2$, $^3P_0 \rightarrow {}^3F_2$, $^3P_1 \rightarrow {}^3F_3$, $^3P_1 \rightarrow {}^3F_4$, $^3P_0 \rightarrow {}^3F_4$, and $^1D_2 \rightarrow {}^3F_2$, respectively.[53,54] Notably, the most intense transition corresponds to $^3P_0 \rightarrow {}^3F_2$. The inset in Fig. 3a shows the transitions originating from $^3P_1$ to $^3F_3$ and $^3F_4$. Additionally, the band detected at 919–1051 nm is attributed to Yb^{3+}, corresponding to the $^2F_{5/2} \rightarrow {}^2F_{7/2}$ transition.[55]

The temporal evolution curve of the $^3P_0$ state in $Y_2Mo_3O_{12}$: 2% Pr^{3+}/15% Yb^{3+} recorded with λ_{ex} = 457 nm and λ_{em} = 980 nm are shown in Fig. 3b. The luminescence decay curve is well fitted using the following function

$$\tau = \frac{\int tI\,\mathrm{d}t}{\int I\,\mathrm{d}t} \qquad (1)$$

where t is the time and $I(t)$ is the emission intensity.

A very fast rise time (0.71 µs) and a long decay time (about 49 µs) were observed. This temporal evolution is indicative of a very fast cross relaxation channel that populates the excited state of Yb^{3+} ions and is given by

$$^1D_2(Pr^{3+}),\ ^2F_{7/2}(Yb^{3+}) > {}^3F_{3,4}(Pr^{3+}),\ ^2F_{5/2}(Yb^{3+})$$

To elucidate the involved down-conversion emission mechanism, the energy level diagram of Pr^{3+} and Yb^{3+} co-doped $Y_2Mo_3O_{12}$ excited at 457 nm is presented in Fig. 4. The excitation of the Pr^{3+} ion occurs from the $^3H_4$ to the $^3P_2$ level. Subsequently, a three process energy transfer from Pr^{3+} to Yb^{3+} is required.[56,57]

Process (1):

$$^3P_0(Pr^{3+}) + {}^2F_{7/2}(Yb^{3+}) \rightarrow {}^1G_4(Pr^{3+}) + {}^2F_{5/2}(Yb^{3+})$$

(1) The effective non-radiative transition of excitation energy from Pr^{3+} to Yb^{3+} ions are caused by the close proximity of the

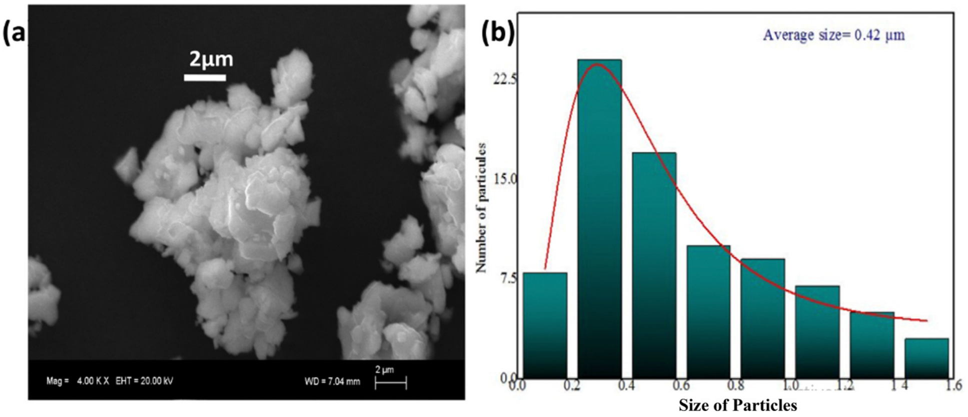

Fig. 2 (a) SEM image and (b) grain size distribution of the synthesized $Y_2Mo_3O_{12}$:2% Pr^{3+}/15% Yb^{3+} phosphor.

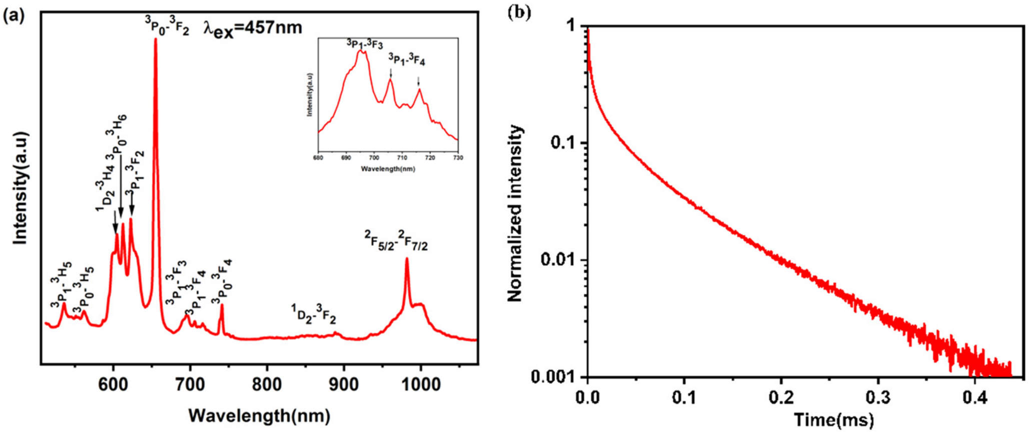

Fig. 3 (a) Visible emission spectrum measured at room temperature upon 457 nm excitation. (b) The temporal evolution in $Y_2Mo_3O_{12}$:2% Pr^{3+}/15% Yb^{3+} measured at 980 nm under 457 nm laser excitation.

energies of $^3P_0$–$^1G_4$ transition in Pr^{3+} ions and the $^2F_{7/2}$–$^2F_{5/2}$ transition in Yb^{3+} ions.

Process (2):

$$^3P_0(Pr^{3+}) \rightarrow {}^2F_{5/2}(Yb^{3+}) + {}^2F_{5/2}(Yb^{3+})$$

(2) Non-radiative excitation decay $^3P_0 \rightarrow {}^3H_4$ of Pr^{3+} ions lead to the simultaneous transfer of excitation energy from the $^3P_0$ level to the two excited Yb^{3+} ions in the $^2F_{5/2}$ states.

Process (3):

(3) Exchange of excitation energy between Pr^{3+} ions can also occur. It is also feasible for there to be a cross-relaxation process between Pr^{3+} and Yb^{3+} ions as a result of the reverse energy transfer from Yb^{3+} to Pr^{3+} ions, which could further contribute to a decrease in the intensity. To obtain the efficient Yb^{3+} luminescence given by process (1) and (3), it is obligatory to populate the $^3P_0$ level of Pr^{3+} ions. This can be practiced by the 457 nm excitation of the $^3H_4 \rightarrow {}^3P_2$ band of Pr^{3+} ions with relaxation to the $^3P_0$ level.

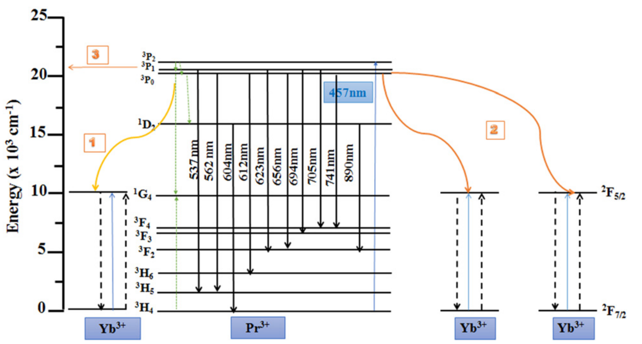

Fig. 4 Schematic energy level diagram for $Y_2Mo_3O_{12}$ codoped Pr^{3+}/Yb^{3+} proposed down emission mechanism under 457 nm excitation.

3. Temperature sensing behaviour

To fully understand the phenomenon of optical thermometry, a thorough theoretical explanation is necessary. Optical thermometry relies on temperature-dependent variations in optical characteristics such as luminescence intensity, wavelength, or lifetime. These variations arise from the temperature-dependent interactions between electrons and phonons, which can lead to spectral broadening and energy level shifts. Higher temperatures increase phonon populations and electron–phonon interactions, causing notable changes in the emission intensity for certain transitions. Thermal quenching, where luminescence efficiency decreases as the temperature increases due to competing non-radiative processes, also plays a role. Materials with larger energy gaps are more susceptible to thermal quenching. Materials with larger energy gaps between the excited and ground states are generally more susceptible to thermal quenching. This increased susceptibility arises because thermal energy, especially at elevated temperatures, can activate non-radiative relaxation pathways. In materials with a large energy gap, the phonon energy becomes sufficient to bridge this gap, enabling phonon-assisted transitions that bypass radiative emission. As a result, non-radiative decay processes dominate, leading to a significant reduction in the luminescent efficiency. Therefore, while large energy gaps are often advantageous for preventing reabsorption or cross-relaxation effects, they pose a challenge for thermal stability. This relationship highlights the need for optimizing the energy gap to balance luminescence efficiency and thermal robustness, particularly for applications requiring stable performance over a range of temperatures.

Additionally, band gaps in semiconductors and insulators tend to narrow with rising temperatures, affecting the photon energy and emission spectra. Excited state lifetimes and dynamics are also temperature-dependent, with higher temperatures typically leading to shorter lifetimes due to increased non-radiative decay rates. In some materials, heat activation can produce higher-lying states with distinct emission properties. Furthermore, temperature-dependent energy transfer between dopant ions can influence the emission peaks and intensities. The temperature sensitivity of radiative transitions in optical thermometry is driven by non-radiative decay processes, the material's band structure, and interactions between electronic states and lattice vibrations. Understanding these underlying mechanisms is crucial for effectively using optical thermometry in practical applications.

In order to investigate the temperature effect, photoluminescence emission spectra were recorded at different temperatures within the range of 298–448 K, as depicted in Fig. 5a. The peak positions remain unchanged by increasing the temperature. To prove the unchanged position of the emission peaks in modified temperature conditions, the normalized emission spectra are shown in Fig. S3 (ESI†). On the other hand, their intensities decrease with increasing temperature. There is a noticeable change in colour from red to orange when the temperature is increased. This variation is shown in the CIE chromaticity diagram presented in Fig. 5b.

As the temperature increases from 298 K to 448 K, the colour coordinates shift from ($x = 0.57, y = 0.41$) to ($x = 0.53, y = 0.45$). It

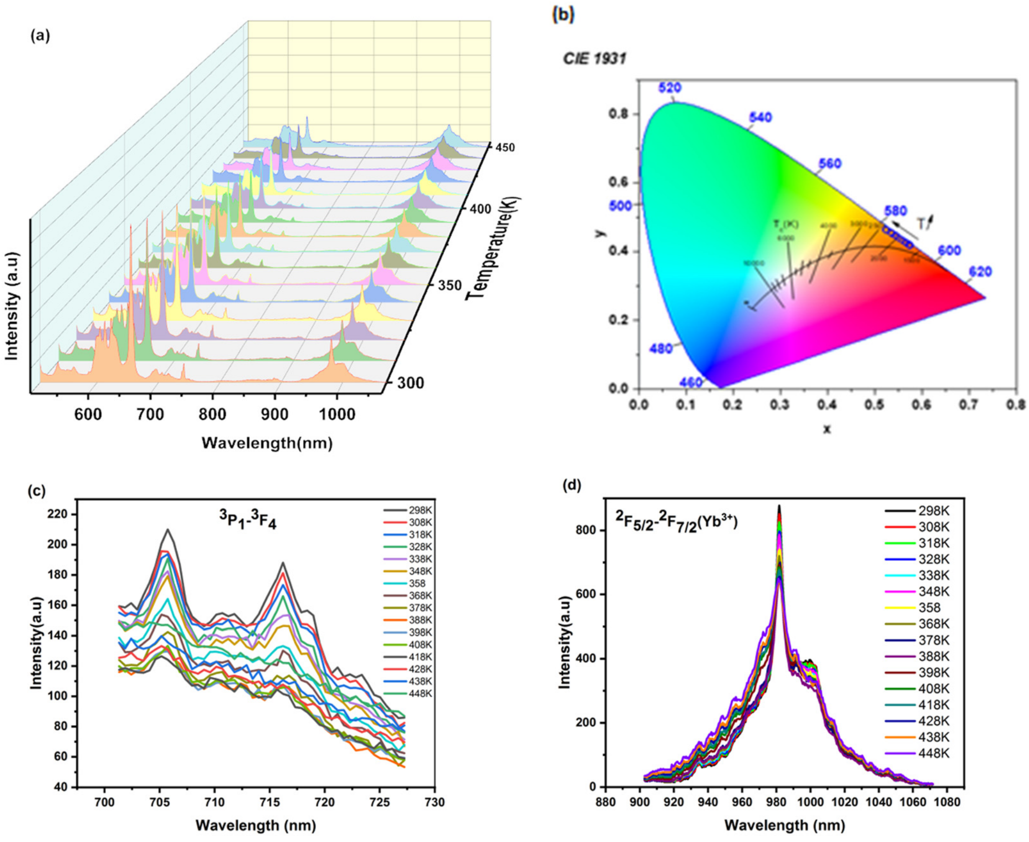

Fig. 5 (a) Temperature dependence of down-conversion emission spectra of $Y_2Mo_3O_{12}$:2% Pr^{3+}/15% Yb^{3+}. (b) CIE coordinate changes with respect to temperature from 298 to 448 K under 457 nm excitation. (c) Temperature dependence of $^3P_1$–$^3F_4$ emission in $Y_2Mo_3O_{12}$:2% Pr^{3+}/15% Yb^{3+}. (d) Temperature dependence of $^2F_{5/2}$–$^2F_{7/2}$ emission in $Y_2Mo_3O_{12}$:2% Pr^{3+}/15% Yb^{3+}.

is clear from the PL spectra that some transitions exhibit a strong and noticeable temperature dependency. Consequently, when the ambient temperature around the phosphor increases, the level of non-radiative relaxation also increases. While the emission peak intensities fall for all transitions, the rate of decrease with temperature varies among them. The peak detected at 623 nm exhibits a faster decline in intensity compared to the 604 nm and 705 nm peaks. The evolution of the intensity of ($^3P_1$–$^3F_4$) as a function of temperature is described in Fig. 5c. The ($^3P_1$–$^3F_4$) peaks decreased with increasing temperature. On the other hand, the temperature dependence of $^2F_{5/2}$–$^2F_{7/2}$(Yb^{3+}) detected at 980 nm is shown in Fig. 5d. The 980 nm peak initially decreases and then increases with an increase in temperature.

The migration in the peak intensities corresponding to the transitions from the $^3P_1$ state is larger than that of the $^3P_0$ state due of thermal agitation.[58] While exciting with the 457 nm light, these energy levels, one is thermally coupled up level and another thermally coupled low level, may be filled and depopulated, respectively, by varying the temperature. The fluorescence intensity ratio FIR from the TCL can be calculated using the Boltzmann distribution theory.[59]

$$\mathrm{FIR_{TCL}} = A\exp\left(\frac{-\Delta E}{k_\mathrm{B}T}\right) \tag{2}$$

where A is a constant, k_B is the Boltzmann constant (k_B = 0.695 K^{-1} cm^{-1}), ΔE is the energy gap separating the two thermalized levels and T represents the absolute temperature. Using eqn (2), we were able to get very accurate results (R = 1) for the calculated band intensity ratios (FIR) corresponding to FIR$_1$ I($^3P_1 \rightarrow {}^3F_4$)/I($^3P_0 \rightarrow {}^3H_6$). These were accomplished by calculating the integrated areas beneath the relevant band. The plots fitted and the experimental values of A and $\Delta E/k_\mathrm{B}$ are shown in Fig. 6. The FIR$_1$ (I_{705}/I_{623}) increases exponentially with temperature. The computed difference in energy (ΔE) between the TCL FIR$_1$ is ΔE = 1583 cm^{-1}.

To objectively analyse the efficacy of temperature sensing based on the associated band ratios, we have calculated their absolute sensitivity (S_a) and relative sensitivity (S_r). S_r is considered a crucial measure for evaluating the performance of temperature sensing in practical applications. This strongly depends on the fitting of the energy difference between the barycentre of the thermalized levels. These parameters can be expressed by eqn (3) and (4).[60–62]

$$S_\mathrm{a} = \frac{\partial \mathrm{FIR}}{\partial T} \tag{3}$$

$$S_\mathrm{r} = 100\% \times \frac{1}{\mathrm{FIR}}\frac{\partial \mathrm{FIR}}{\partial T} \tag{4}$$

Accordingly, the calculated S_a and S_r values of FIR$_1$ at diverse temperatures are shown in Fig. 7. It can be seen that S_r decreases with the increase in temperature. The highest values S_a and S_r of FIR$_1$ are equal to 2.2010^{-5} K^{-1} (at 448 K) and 2.61% K^{-1} (at 298 K), respectively.

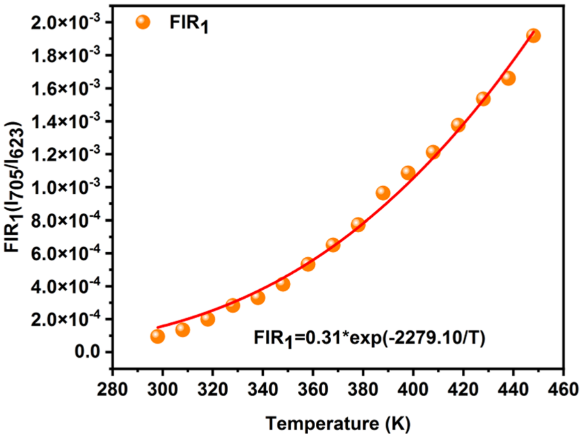

Fig. 6 Plots of FIR$_1$ based on thermally coupled levels.

The study showed that Pr^{3+} ions have the potential to be used as thermometers in luminescence thermometry. This is achieved using the luminescence intensity ratio (FIR) of two thermally linked electron levels of Pr^{3+} ions when they are optically excited to the $^3P_0$ level. The samples exhibited greater temperature sensitivity compared to other materials doped with Ho^{3+}/Yb^{3+} (ref. 63) and Er^{3+}/Yb^{3+}.[47] The temperature mapping of microcircuits and biomedical *in vitro* applications are both facilitated by these systems. However, the temperature sensitivity is not the only characteristic of luminescence thermometers. Critical parameters such as the excitation wavelength, luminescence spectral range, and luminescence quantum yield are equally significant. Specifically, for biological applications, infrared excitation is critical because it prevents cells and tissues from fluorescing automatically. For the temperature measurement of microcircuits, the excitation wavelength is not such a limiting parameter and the choice of the luminescence sensors depends on a specific assignment. According to eqn (2), the sensitivity for TCLs is proportional to the energy gap ΔE at a specific temperature. In other words, substantial ΔE is conducive to high sensitivity. However, the ΔE between the TCLs should be larger than 200 cm^{-1} but lower than 2000 cm^{-1}. As

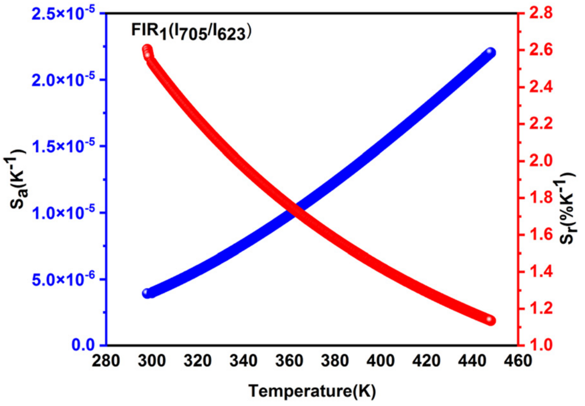

Fig. 7 Relative and absolute sensitivities S_r and S_a based on the TCLs FIR$_1$ of Pr^{3+}/Pr^{3+} as a function of temperature.

a result, the sensitivity for the FIR method applying TCLs is theoretically restricted. However, the NTCLs without energy restriction may occur between the same or co-doped two distinct luminescent ions, which indicate that more energy level combinations can be employed to make multichannel temperature monitoring feasible. Thus, the abundance of emission bands across a broad range in our materials is suited for NTCLs temperature measuring application. It is stated that the $\mathrm{FIR_{NTCLs}}$ vs the temperature may be fitted to a polynomial function[14,64,65]

$$\mathrm{FIR_{NTCL}} = A + BT + CT^2 + DT^3 \qquad (5)$$

where A, B, C and D represent the fitting parameters. We investigate the intensity ratios of $\mathrm{FIR_2}$ $\mathrm{I(^3P_1 \rightarrow {}^3F_4)/I(^1D_2 \rightarrow {}^3F_2)}$ and $\mathrm{FIR_3}$ $\mathrm{I(^3P_1 \rightarrow {}^3F_4)/I(^2F_{5/2} \rightarrow {}^2F_{7/2})}$ in $\mathrm{Y_2Mo_3O_{12}{:}Pr^{3+}/Yb^3}$ phosphor within the framework of the FIR technique for Non-Thermally Coupled Levels (NTCLs). The experimental data for $\mathrm{FIR_{NTCLs}}$ are fitted (Fig. 8(a) and (b)) and thermometry coefficients A, B, C and D are collected in Table S1 (ESI†).

The S_a and S_r values obtained for NTCLs $\mathrm{FIR_2}$ (I_{705}/I_{890}) and $\mathrm{FIR_3}$ (I_{705}/I_{980}) are depicted in Fig. 9(a) and (b). The maximum values of S_a and S_r for $\mathrm{FIR_2}$ were found to be about $6.29.10^{-5}$ $\mathrm{K^{-1}}$ (at 384 K) and 3.6% $\mathrm{K^{-1}}$ (at 314 K), respectively (Fig. 9a). The highest S_a and S_r values for $\mathrm{FIR_3}$ are equal to $4.25.10^{-6}$ $\mathrm{K^{-1}}$ and 11.2% $\mathrm{K^{-1}}$, respectively, obtained at 298 K (Fig. 9b).

On the other hand, Table 1 presents a comparative analysis of the thermometric capabilities of phosphors that serve as typical samples from other pertinent studies. Table 1 compiles the relative sensitivities of several materials for optical thermometry and compares them to our phosphor's sensing sensitivity based on TCL and non-TCLs. This comparison underscores the varying levels of maximum relative sensitivity (S_r) for temperature sensing among different phosphors. It may be inferred that the $\mathrm{Y_2Mo_3O_{12}{:}Yb^{3+}/Pr^{3+}}$phosphor displays superior performance compared with prior data. The S_r values at about room temperature are particularly outstanding, which implies that the material may be employed in a broader variety of applications. The NTCLS represented by $\mathrm{FIR_2}$ and $\mathrm{FIR_3}$ have a higher relative sensitivity than TCL represented by $\mathrm{FIR_1}$. The actual potentialities of the $\mathrm{Y_2Mo_3O_{12}{:}Pr^{3+}/Yb^{3+}}$ in the optical thermometry field were consequently confirmed. Bi-centre systems, such as $\mathrm{Y_2Mo_3O_{12}{:}Pr^{3+}/Yb^{3+}}$ nanoparticles, often exhibit higher sensitivity to temperature changes compared to single-centre systems. This enhanced sensitivity allows for more precise and accurate temperature measurements, which are crucial in applications where small variations in temperature need to be detected. Indeed, the use of bi-centre systems such as $\mathrm{Y_2Mo_3O_{12}{:}Pr^{3+}/Yb^{3+}}$ nanoparticles offer improved sensitivity, ratiometric measurements for accuracy, a wide temperature range, robustness against external factors, customization options, and compatibility with optical systems, making them highly advantageous for luminescent thermometry applications. It is noted that the relative sensitivity obtained based on the ratio involving the emissions of one $\mathrm{Pr^{3+}}$ (705 nm) and one $\mathrm{Yb^{3+}}$ (980 nm) provides the highest relative sensitivity 11.2% $\mathrm{K^{-1}}$, indicating superior performance in luminescent thermometry. This observation suggests that using a bi-centre luminescent thermometer offers higher performance compared to a single-centre system.

Another essential parameter for evaluating the performance of an optical thermometer is the temperature uncertainty (δT), which represents the slightest detectable temperature change within a measurement. The δT value can be calculated as follows.[68,69]

$$\delta T = \frac{1}{S_\mathrm{R}}\frac{\delta \mathrm{FIR}}{\mathrm{FIR}} \qquad (6)$$

where δFIR is the uncertainty of the FIR value. To determine the δFIR, 100 measurements were made at room temperature under similar circumstances for $\mathrm{Y_2Mo_3O_{12}{:}2\%\ Pr^{3+}/15\%\ Yb^{3+}}$ upon 457 nm excitation. Herein, δFIR adopts the standard deviation of the FIR data obtained from multiple measurements at a fixed temperature, as shown in Fig. S4(a)–(c) (ESI†).

The δT value was determined to be 0.27 K for $\mathrm{FIR_1}$, 1.42 K for $\mathrm{FIR_2}$ and 0.12 K for $\mathrm{FIR_3}$, respectively, at room temperature, as depicted in Fig. 10(a)–(c). Considering the high sensing sensitivity, low temperature uncertainty and the application of dual-FIR data, we suggest that the $\mathrm{Y_2Mo_3O_{12}{:}Pr^{3+}/Yb^{3+}}$phosphor could be implemented in optical thermometry with brilliant applications.

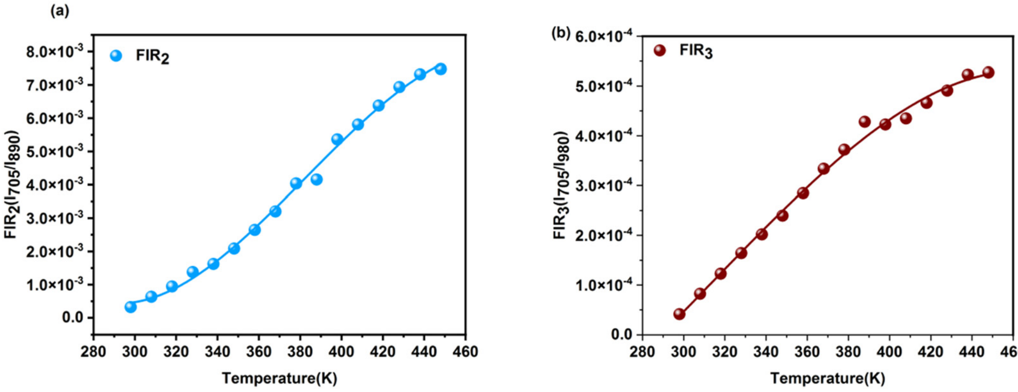

Fig. 8 Plot of FIR based on non-thermally coupled levels: (a) $\mathrm{FIR_2}$, (b) $\mathrm{FIR_3}$ and the corresponding fitting according eqn (5) as a function of temperature.

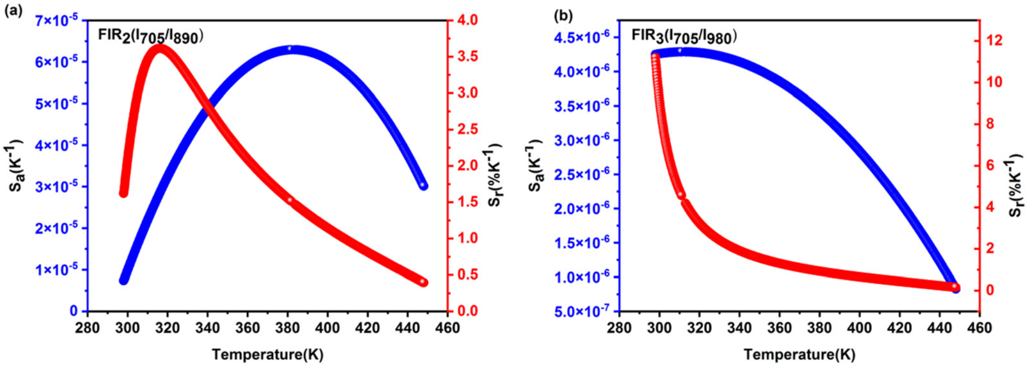

Fig. 9 The calculated S_r and S_a values based on non-TCLs of (a) FIR_2 and (b) FIR_3 as a function of temperature.

Table 1 The calculated maximum relative sensor sensitivities (S_{rmax}) and the corresponding transitions of $Y_2Mo_3O_{12}$:2% Pr^{3+}/15% Yb^{3+}

Phosphors	Emission	S_{rmax} (% K^{-1})	Ref.
$Y_2Mo_3O_{12}:Pr^{3+}/Yb^{3+}$	705/623 (FIR_1)	2.61	This work
	705/890 (FIR_2)	3.6	
	705/980 (FIR_3)	11.2	
$Bi_4Ti_3O_{12}:Pr^{3+}/Yb^{3+}$	545/623	0.68	66
$Y_2Mo_4O_{15}:Pr^{3+}/Yb^{3+}$	980/490	1.15	42
	547/490	1.27	
	980/490	1.15	
$LaF_3:Pr^{3+},Yb^{3+}$	—	1.08	67
PMN-PT:Pr^{3+},Yb^{3+}	608/490	1.03	26

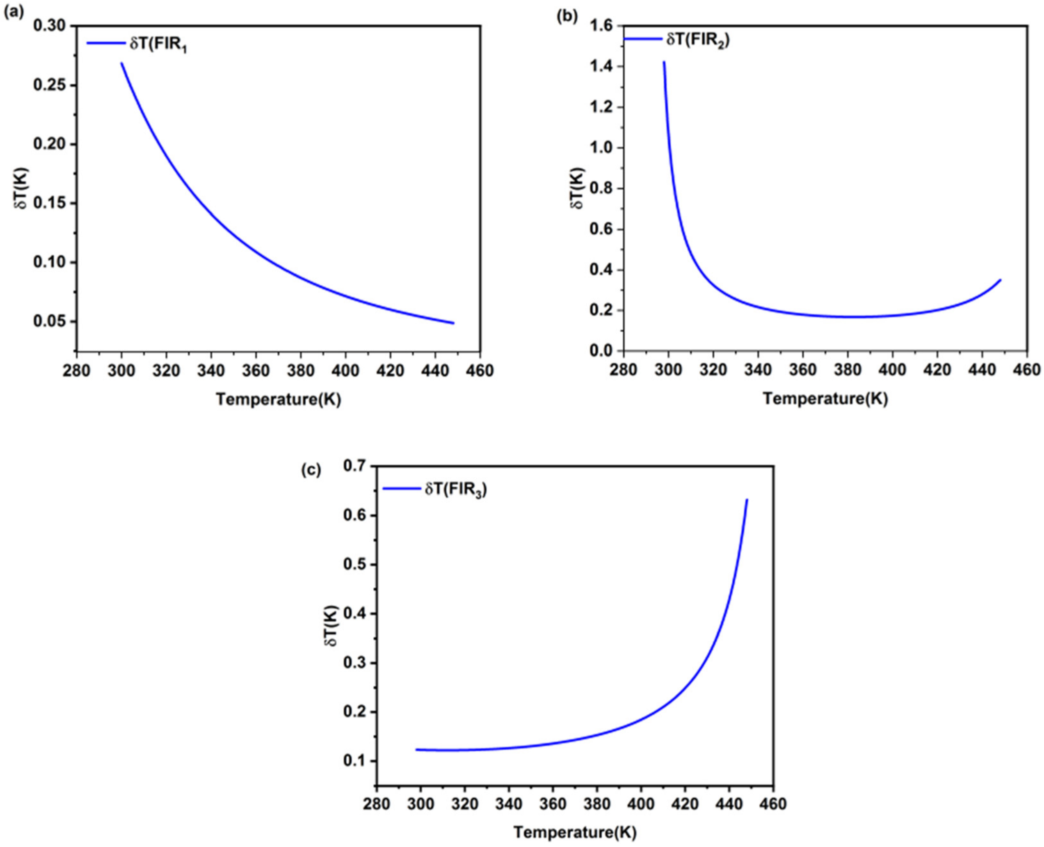

Fig. 10 Temperature uncertainty values (δ*T*) for (a) FIR_1, (b) FIR_2, and (c) FIR_3.

V. Conclusion

In this work, we delve into the synthesis and characterization of $Y_2Mo_3O_{12}$:Pr^{3+}/Yb^{3+} nanoparticles for non-contact luminescent thermometry, an area garnering significant attention due to its diverse applications in varied environments. Yb^{3+}/Pr^{3+} co-doped $Y_2Mo_3O_{12}$ was successfully synthesized by the sol–gel method. Photoluminescence proves to be sensitive to temperature variations. Through meticulous evaluation utilizing X-ray diffraction (XRD), scanning electron microscopy (SEM), and photoluminescence (PL) techniques, we explored the luminescent properties of these nanoparticles, observing intense emissions from excited states such as $^3P_0$, $^1G_4$, and $^1D_2$ upon excitation with 457 nm light. Our investigations span temperatures from 298 K to 448 K, revealing the high sensitivity of $Y_2Mo_3O_{12}$:Pr^{3+}/Yb^{3+} nanoparticles in temperature sensing, notably achieving a maximum relative sensitivity of 11.2% K^{-1} at 298 K. Additionally, we analysed the thermal and non-thermal coupling levels of Pr^{3+} and Yb^{3+} ions using the fluorescence intensity ratio (FIR) technique, unveiling promising results. This work underscores the potential of $Y_2Mo_3O_{12}$:Pr^{3+}/Yb^{3+} nanoparticles in optical thermometry, showcasing their effectiveness as temperature sensors across a wide range of environments. Our findings indicate that utilizing bi-center luminescent thermometers, particularly the $Y_2Mo_3O_{12}$:Pr^{3+}/Yb^{3+} system, offers superior performance compared to single-center systems, paving the way for precise, reliable, and versatile temperature measurements across various applications in optical thermometry.

Data availability

All data underlying the results are available as part of the article, and no additional source data are required.

Conflicts of interest

The authors declare no competing financial interest.

Acknowledgements

This work was supported by the Ministry of Higher Education and Scientific Research Tunisia and by Ministerio de Ciencia e Innovacion of Spain (MICIIN) under the National Program of Sciences and Technological Materials (PID2019-106383GB-C44 and PID2019-107335RA-I00) and EU-FEDER funds.

References

1 S. Goderski, M. Runowski, P. Woźny, V. Lavín and S. Lis, Lanthanide Upconverted Luminescence for Simultaneous Contactless Optical Thermometry and Manometry–Sensing under Extreme Conditions of Pressure and Temperature, *ACS Appl. Mater. Interfaces*, 2020, **12**, 40475–40485, DOI: **10.1021/acsami.0c09882**.

2 M. K. Hossain, S. Hossain, M. H. Ahmed, M. I. Khan, N. Haque and G. A. Raihan, A Review on Optical Applications, Prospects, and Challenges of Rare-Earth Oxides, *ACS Appl. Electron. Mater.*, 2021, **3**, 3715–3746, DOI: **10.1021/acsaelm.1c00682**.

3 Y. Gao, F. Huang, H. Lin, J. Zhou, J. Xu and Y. Wang, A Novel Optical Thermometry Strategy Based on Diverse Thermal Response from Two Intervalence Charge Transfer States, *Adv. Funct. Mater.*, 2016, **26**, 3139–3145, DOI: **10.1002/adfm.201505332**.

4 M. Runowski, P. Woźny, S. Lis, V. Lavín and I. R. Martín, Optical Vacuum Sensor Based on Lanthanide Upconversion—Luminescence Thermometry as a Tool for Ultralow Pressure Sensing, *Adv. Mater. Technol.*, 2020, **5**, 1901091, DOI: **10.1002/admt.201901091**.

5 K. Soler-Carracedo, I. R. Martín, F. Lahoz, H. C. Vasconcelos, A. D. Lozano-Gorrín, L. L. Martín and F. Paz-Buclatin, Er^{3+}/Ho^{3+} codopednanogarnet as an optical FIR based thermometer for a wide range of high and low temperatures, *J. Alloys Compd.*, 2020, **847**, 156541, DOI: **10.1016/j.jallcom.2020.156541**.

6 T. Zheng, M. Runowski, P. Woźny, B. Barszcz, S. Lis, M. Vega, J. Llanos, K. Soler-Carracedo and I. R. Martín, Boltzmann vs. non-Boltzmann (non-linear) thermometry – Yb^{3+}–Er^{3+} activated dual-mode thermometer and phase transition sensor via second harmonic generation, *J. Alloys Compd.*, 2022, **906**, 164329, DOI: **10.1016/j.jallcom.2022.164329**.

7 K. Saidi, M. Yangui, C. Hernández-Álvarez, M. Dammak, I. Rafael Martín Benenzuela and M. Runowski, Multifunctional Optical Sensing with Lanthanide-Doped Upconverting Nanomaterials: Improving Detection Performance of Temperature and Pressure in the Visible and NIR Ranges, *ACS Appl. Mater. Interfaces*, 2024, **16**, 19137–19149, DOI: **10.1021/acsami.4c00313**.

8 M. Colombo, S. Carregal-Romero, M. F. Casula, L. Gutiérrez, M. P. Morales, I. B. Böhm, J. T. Heverhagen, D. Prosperi and W. J. Parak, Biological applications of magnetic nanoparticles, *Chem. Soc. Rev.*, 2012, **41**, 4306, DOI: **10.1039/c2cs15337h**.

9 B. del Rosal, I. Villa, D. Jaque and F. Sanz-Rodríguez, *In vivo* autofluorescence in the biological windows: the role of pigmentation, *J. Biophotonics*, 2016, **9**, 1059–1067, DOI: **10.1002/jbio.201500271**.

10 Y. Chen, T. Tran, H. Duong, C. Li, M. Toth, C. Bradac, I. Aharonovich, A. Solntsev and T. Tran, Optical Thermometry with Quantum Emitters in Hexagonal Boron Nitride, *ACS Appl. Mater. Interfaces*, 2020, **12**, 25464–25470, DOI: **10.48550/arXiv.2003.03869**.

11 Y. Chen, C. Li, T. Yang, E. Ekimov, C. Bradac, M. Toth, I. Aharonovich and T. Tran, Real-time ratiometric optical nanoscale thermometry, *ACS Nano*, 2023, **17**(3), 2725–2736, DOI: **10.48550/arXiv.2112.01758**.

12 O. A. Savchuk, J. J. Carvajal, C. Cascales, J. Massons, M. Aguiló and F. Díaz, Thermochromic upconversion nanoparticles for visual temperature sensors with high thermal, spatial and temporal resolution, *J. Mater. Chem. C*, 2016, **4**, 6602–6613, DOI: **10.1039/C6TC01841F**.

13 Z. Cheng, J. Lu, Z. Li, M. Meng, X. Qiao, Y. Liu and J. Ou, Promising lanthanide-$NaYbF_4$:Er^{3+}@$NaYbF_4$:Tm^{3+}

micro-phosphors for highly efficient upconversion luminescence and temperature sensing, *Opt. Mater.*, 2024, **154**, 115675, DOI: **10.1016/j.optmat.2024.115675**.

14 K. Saidi, C. Hernández-Álvarez, M. Runowski, M. Dammak and I. Rafael Martín Benenzuela, Temperature and Pressure Sensing Using an Optical Platform Based on Upconversion Luminescence in NaSrY$(MoO_4)_3$ Codoped with Er^{3+} and Yb^{3+} Nanophosphors, *ACS Appl. Nano Mater.*, 2023, **6**, 19431–19442, DOI: **10.1021/acsanm.3c04031**.

15 H. Lv, P. Du, W. Li and L. Luo, Tailoring of Upconversion Emission in Tm^{3+}/Yb^{3+}-Codoped $Y_2Mo_3O_{12}$ Submicron Particles Via Thermal Stimulation Engineering for Non-invasive Thermometry, *ACS Sustainable Chem. Eng.*, 2022, **10**, 2450–2460, DOI: **10.1021/acssuschemeng.1c07323**.

16 A. I. Becerro, M. Allix, M. Laguna, D. González-Mancebo, C. Genevois, A. Caballero, G. Lozano, N. O. Núñez and M. Ocaña, Revealing the substitution mechanism in $Eu^{3+}:CaMoO_4$ and $Eu^{3+},Na^{+}:CaMoO_4$ phosphors, *J. Mater. Chem. C*, 2018, **6**, 12830–12840, DOI: **10.1039/C8TC04595J**.

17 Z. E. A. A. Taleb, K. Saidi, M. Dammak, D. Przybylska and T. Grzyb, Ultrasensitive optical thermometry using Tb^{3+} doped NaSrGd$(MoO_4)_3$ based on single band ratiometric luminescence, *Dalton Trans.*, 2023, **52**, 4954–4963, DOI: **10.1039/D3DT00376K**.

18 Z. Liu and R. X. Wang, Luminescence thermometry based on downshifting and upconversion photoluminescence of $Bi_4Ti_3O_{12}:Yb^{3+}/Pr_{3+}$ ceramic, *Chalcogenide Lett.*, 2022, **19**, 471, DOI: **10.15251/CL.2022.197.471**.

19 W. Ye, C. Ma, Y. Li, C. Zhao, Y. Wang, C. Zuo, Z. Wen, Y. Li, X. Yuan and Y. Cao, Anti-thermal-quenching red-emitting $GdNbO_4:Pr^{3+}$ phosphor based on metal-to-metal charge transfer for optical thermometry application, *J. Mater. Chem. C*, 2021, **9**, 15201–15211, DOI: **10.1039/D1TC03978D**.

20 Z. E. A. A. Taleb, K. Saidi and M. Dammak, Dual-mode optical ratiometric thermometry using Pr^{3+}-doped NaSrGd$(MoO_4)_3$ phosphors with tunable sensitivity, *Dalton Trans.*, 2023, **52**, 18069–18081, DOI: **10.1039/D3DT03242F**.

21 J. Stefanska, K. Maciejewska and L. Marciniak, Blue-emitting single band ratiometric luminescent thermometry based on $LaF_3:Pr^{3+}$, *New J. Chem.*, 2021, **45**, 11898–11904, DOI: **10.1039/D1NJ01869H**.

22 F. Jahanbazi, Y. Wang, J. A. Dorman and Y. Mao, $La_2Zr_2O_7:Pr^{3+}$ nanoparticles for luminescence thermometry based on a single parameter over a wide temperature range of 620 K, *J. Alloys Compd.*, 2022, **911**, 165013, DOI: **10.1016/j.jallcom.2022.165013**.

23 W. Lozano B, C. B. de Araújo, C. Egalon, A. S. L. Gomes, B. J. Costa and Y. Messaddeq, Upconversion of infrared-to-visible light in Pr^{3+}–Yb^{3+} codopedfluoroindate glass, *Opt. Commun.*, 1998, **153**, 271–274, DOI: **10.1016/S0030-4018(98)00268-5**.

24 W. Wang, Y. Xue, J. Dong, C. Zhang, J. Liu, W. Hou, Q. Wang, X. Xu, H. Tang, H. Lin, D. Li, Z. Wang and J. Xu, Yb^{3+} sensitization effect to Pr^{3+} originated from $^1G_4$ level broadband near-infrared emission and up-conversion in BaF_2 crystal, *Opt. Mater. Express*, 2023, **13**, 1267–1277, DOI: **10.1364/OME.471546**.

25 Q. Zhang, L. Luo, Z. Zhu, P. Du and Y. Zhang, Reversible luminescence modulation and temperature-sensing properties of Pr^{3+}/Yb^{3+} codoped $K_{0.5}Na_{0.5}NbO_3$ ceramics, *J. Am. Ceram. Soc.*, 2019, **102**, 6018–6026, DOI: **10.1111/jace.16480**(n.d.).

26 L. Bi, J. Fu, Z. Lv, Z. Luo and C. Lu, Temperature-dependent upconversion luminescence in ferroelectric 1.5% Pr/3% $Yb:0.75Pb(Mg_{1/3}Nb_{2/3})O_3–0.25PbTiO_3$ transparent ceramics for non-contact thermometry and optical heating, *Ceram. Int.*, 2020, **46**, 13407–13413, DOI: **10.1016/j.ceramint.2020.02.123**.

27 I. Kachou, K. Saidi, R. Salhi and M. Dammak, Synthesis and optical spectroscopy of $Na_3Y(VO_4)_2:Eu^{3+}$ phosphors for thermometry and display applications, *RSC Adv.*, 2022, **12**, 7529–7539, DOI: **10.1039/D2RA00539E**.

28 K. Saidi and M. Dammak, Upconversion luminescence and optical temperature sensing characteristics of Er^{3+}/Yb^{3+} codoped $Na_3Gd(PO_4)_2$ phosphors, *J. Solid State Chem.*, 2021, **300**, 122214, DOI: **10.1016/j.jssc.2021.122214**.

29 K. Saidi, C. Hernández-Álvarez, M. Runowski, M. Dammak and I. Benenzuela, Temperature and Pressure Sensing Using an Optical Platform Based on Upconversion Luminescence in NaSrY$(MoO_4)_3$ Codoped with Er^{3+} and Yb^{3+} Nanophosphors, *ACS Appl. Nano Mater.*, 2023, **6**, 19431–19442, DOI: **10.1021/acsanm.3c04031**.

30 F. Ayachi, K. Saidi, W. Chaabani and M. Dammak, Synthesis and luminescence properties of Er^{3+} doped and Er^{3+}–Yb^{3+} codopedphosphovanadate $YP_{0.5}V_{0.5}O_4$ phosphors, *J. Lumin.*, 2021, **240**, 118451, DOI: **10.1016/j.jlumin.2021.118451**.

31 I. Kachou, M. Dammak, S. Auguste, F. Amiard and P. Daniel, A novel optical temperature sensor and energy transfer properties based on Tb^{3+}/Sm^{3+} codoped $SrY_2(MoO_4)_4$ phosphors, *Dalton Trans.*, 2023, **52**, 18233–18246, DOI: **10.1039/d3dt03410k**.

32 K. Saidi, I. Kachou, K. Soler-Carracedo, M. Dammak and I. Martin, $Ba_2YV_3O_{11}Er^{3+}/Yb^{3+}$ Nanostructures for Temperature Sensing in the Presence of Bismuth Ions, *ACS Appl. Nano Mater.*, 2023, **6**, 17681–17690, DOI: **10.1021/acsanm.3c02911**.

33 M. Monika, R. S. Yadav, A. Bahadur and S. B. Rai, Concentration and pump power-mediated color tunability, optical heating and temperature sensing *via* TCLs of red emission in an $Er^{3+}/Yb^{3+}/Li^{+}$ co-doped $ZnGa_2O_4$ phosphor, *RSC Adv.*, 2019, **9**, 40092–40108, DOI: **10.1039/C9RA09120C**.

34 M. Jia, Z. Sun, H. Xu, X. Jin, Z. Lv, T. Sheng and Z. Fu, An ultrasensitive luminescent nanothermometer in the first biological window based on phonon-assisted thermal enhancing and thermal quenching, *J. Mater. Chem. C*, 2020, **8**, 15603–15608, DOI: **10.1039/D0TC04082G**.

35 M. Runowski, Pressure and temperature optical sensors: luminescence of lanthanide-doped nanomaterials for contactless nanomanometry and nanothermometry, *Handbook of Nanomaterials in Analytical Chemistry*, Elsevier, 2020, pp. 227–273. , DOI: **10.1016/B978-0-12-816699-4.00010-4**.

36 P. Du, L. Luo, H.-K. Park and J. S. Yu, Citric-assisted sol-gel based Er^{3+}/Yb^{3+}-codoped $Na_{0.5}Gd_{0.5}MoO_4$: a novel

highly-efficient infrared-to-visible upconversion material for optical temperature sensors and optical heaters, *Chem. Eng. J.*, 2016, **306**, 840–848, DOI: **10.1016/j.cej.2016.08.007**.

37 S. Sinha, M. K. Mahata, K. Kumar, S. P. Tiwari and V. K. Rai, Dualistic temperature sensing in Er^{3+}/Yb^{3+} doped $CaMoO_4$ upconversion phosphor, *Spectrochim. Acta, Part A*, 2017, **173**, 369–375, DOI: **10.1016/j.saa.2016.09.039**.

38 R. L. Tranquilin, L. X. Lovisa, C. R. R. Almeida, C. A. Paskocimas, M. S. Li, M. C. Oliveira, L. Gracia, J. Andres, E. Longo, F. V. Motta and M. R. D. Bomio, Understanding the White-Emitting $CaMoO_4$ Co-Doped Eu^{3+}, Tb^{3+}, and Tm^{3+} Phosphor through Experiment and Computation, *J. Phys. Chem. C*, 2019, **123**, 18536–18550, DOI: **10.1021/acs.jpcc.9b04123**.

39 L. Li, P. Yang, W. Xia, Y. Wang, F. Ling, Z. Cao, S. Jiang, G. Xiang, X. Zhou and Y. Wang, Luminescence and optical thermometry strategy based on emission and excitation spectra of Pr^{3+} doped $SrMoO_4$ phosphors, *Ceram. Int.*, 2021, **47**, 769–775, DOI: **10.1016/j.ceramint.2020.08.187**.

40 Pushpendra, R. K. Kunchala, R. Kalia and B. S. Naidu, Upconversion luminescence properties of $NaBi(MoO_4)_2:Ln^{3+},Yb^{3+}$ (Ln = Er, Ho) nanomaterials synthesized at room temperature, *Ceram. Int.*, 2020, **46**, 18614–18622, DOI: **10.1016/j.ceramint.2020.04.173**.

41 C. S. Lim, A. Aleksandrovsky, M. Molokeev, A. Oreshonkov and V. Atuchin, The modulated structure and frequency upconversion properties of $CaLa_2(MoO_4)_4:Ho^{3+}/Yb^{3+}$ phosphors prepared by microwave synthesis, *Phys. Chem. Chem. Phys.*, 2015, **17**, 19278–19287, DOI: **10.1039/C5CP03054D**.

42 M. Fhoula, K. Saidi, C. Hernández-Álvarez, K. Soler-Carracedo, M. Dammak and I. R. Martín, Unlocking the luminescent potential of Pr^{3+}/Yb^{3+} Co-doped $Y_2Mo_4O_{15}$ for advanced thermometry applications, *J. Alloys Compd.*, 2024, **979**, 173537, DOI: **10.1016/j.jallcom.2024.173537**.

43 P. Du, L. Luo, Y. Hou and W. Li, Energy transfer-triggered multicolor emissions in Tb^{3+}/Eu^{3+}-coactivated $Y_2Mo_3O_{12}$ negative thermal expansion microparticles for dual-channel tunable luminescent thermometers, *Mater. Adv.*, 2021, **2**, 4824–4831, DOI: **10.1039/D1MA00218J**.

44 X. Liu, Y. Cheng, E. Liang and M. Chao, Interaction of crystal water with the building block in $Y_2Mo_3O_{12}$ and the effect of Ce^{3+} doping, *Phys. Chem. Chem. Phys.*, 2014, **16**, 12848–12857, DOI: **10.1039/C4CP00144C**.

45 Y. Yang, L. Lin, P. Lu, Z. Feng, Z. Li, J. Cai, Z. Mei, Y. Huang, W. Guo, Z. Wang and Z. Zheng, A linear calibrated high temperature sensor based on up-conversion fluorescence of $Y_2Mo_3O_{12}:Er^{3+},Yb^{3+}$ enhanced by negative thermal expansion, *J. Lumin.*, 2021, **240**, 118410, DOI: **10.1016/j.jlumin.2021.118410**.

46 Y. Zi, Z. Yang, Z. Xu, X. Bai, A. Ullah, I. Khan, A. A. Haider, J. Qiu, Z. Song, Y. Wang and Y. Cun, A novel upconversion luminescence temperature sensing material: negative thermal expansion $Y_2Mo_3O_{12}:Yb^{3+},Er^{3+}$ and positive thermal expansion $Y_2Ti_2O_7:Yb^{3+},Er^{3+}$ mixed phosphor, *J. Alloys Compd.*, 2021, **880**, 160156, DOI: **10.1016/j.jallcom.2021.160156**.

47 H. Lv, P. Du, L. Luo and W. Li, Negative thermal expansion triggered anomalous thermal upconversion luminescence behaviors in Er^{3+}/Yb^{3+}-codoped $Y_2Mo_3O_{12}$ microparticles for highly sensitive thermometry, *Mater. Adv.*, 2021, **2**, 2642–2648, DOI: **10.1039/D1MA00072A**.

48 H. Lv, P. Du, W. Li and L. Luo, Tailoring of Upconversion Emission in Tm^{3+}/Yb^{3+}-Codoped $Y_2Mo_3O_{12}$ Submicron Particles Via Thermal Stimulation Engineering for Non-invasive Thermometry, *ACS Sustainable Chem. Eng.*, 2022, **10**, 2450–2460, DOI: **10.1021/acssuschemeng.1c07323**.

49 Y. Zhang, M. Jin, W. Chen, Z. Wu, Z. Li and C. Guo, Thermally enhanced NIR up-conversion fluorescence multi-mode thermometry based on $Y_2Mo_3O_{12}:Nd^{3+},Yb^{3+}$, *J. Mater. Chem. C*, 2024, **12**, 7588–7595, DOI: **10.1039/D4TC01352B**.

50 E. Liang, H. Huo, J. Wang and M. Chao, Effect of Water Species on the Phonon Modes in Orthorhombic $Y_2(MoO_4)_3$ Revealed by Raman Spectroscopy, *J. Phys. Chem. C*, 2008, **112**, 6577–6581, DOI: **10.1021/jp8013332**.

51 B. A. Marinkovic, P. M. Jardim, R. R. de Avillez and F. Rizzo, Negative thermal expansion in $Y_2Mo_3O_{12}$, *Solid State Sci.*, 2005, **7**, 1377–1383, DOI: **10.1016/j.solidstatesciences.2005.08.012**.

52 R. D. Shannon, Revised effective ionic radii and systematic studies of interatomic distances in halides and chalcogenides, *Acta Crystallogr., Sect. A*, 1976, **32**, 751–767, DOI: **10.1107/S0567739476001551**.

53 M. S. Pudovkin, O. A. Morozov, V. V. Pavlov, S. L. Korableva, E. V. Lukinova, Y. N. Osin, V. G. Evtugyn, R. A. Safiullin and V. V. Semashko, Physical Background for Luminescence Thermometry Sensors Based on $Pr^{3+}:LaF_3$ Crystalline Particles, *J. Nanomater.*, 2017, **2017**, 1–9, DOI: **10.1155/2017/3108586**.

54 S. Jana, A. Mondal, J. Manam and S. Das, Pr^{3+} doped $BaNb_2O_6$ reddish orange emitting phosphor for solid state lighting and optical thermometry applications, *J. Alloys Compd.*, 2020, **821**, 153342, DOI: **10.1016/j.jallcom.2019.153342**.

55 W. Wang, J. Tian, J. Dong, Y. Xue, D. Hu, W. Hou, H. Tang, Q. Wang, X. Xu and J. Xu, Growth, spectroscopic properties and up-conversion of Yb, Pr co-doped CaF_2 crystals, *J. Lumin.*, 2021, **233**, 117931, DOI: **10.1016/j.jlumin.2021.117931**.

56 M. S. Pudovkin, S. V. Kuznetsov, V. Y. Proydakova, V. V. Voronov and V. V. Semashko, Luminescent thermometry based on $Ba_4Y_3F_{17}:Pr^{3+}$ and $Ba_4Y_3F_{17}:Pr^{3+},Yb^{3+}$ nanoparticles, *Ceram. Int.*, 2020, **46**, 11658–11666, DOI: **10.1016/j.ceramint.2020.01.196**.

57 S. V. Kuznetsov, O. A. Morozov, V. G. Gorieva, M. N. Mayakova, M. A. Marisov, V. V. Voronov, A. D. Yapryntsev, V. K. Ivanov, A. S. Nizamutdinov, V. V. Semashko and P. P. Fedorov, Synthesis and luminescence studies of CaF_2:Yb:Pr solid solutions powders for photonics, *J. Fluorine Chem.*, 2018, **211**, 70–75, DOI: **10.1016/j.jfluchem.2018.04.008**.

58 S. Hu, C. Lu, X. Liu and Z. Xu, Optical temperature sensing based on the luminescence from YAG:Pr transparent ceramics, *Opt. Mater.*, 2016, **60**, 394–397, DOI: **10.1016/j.optmat.2016.08.026**.

59 M. S. Pudovkin, D. A. Koryakovtseva, E. V. Lukinova, S. L. Korableva, R. S. Khusnutdinova, A. G. Kiiamov, A. S. Nizamutdinov and V. V. Semashko, Luminescence Nanothermometry Based on $Pr^{3+}:LaF_3$ Single Core and

Pr^{3+}:LaF_3/LaF_3 Core/Shell Nanoparticles, *Adv. Mater. Sci. Eng.*, 2019, **2019**, 1–14, DOI: **10.1155/2019/2618307**.

60 F. Ayachi, K. Saidi, M. Dammak, W. Chaabani, I. Mediavilla-Martínez and J. Jiménez, Dual-mode luminescence of Er^{3+}/Yb^{3+} codoped $LnP_{0.5}V_{0.5}O_4$ (Ln = Y, Gd, La) for highly sensitive optical nanothermometry, *Mater. Today Chem.*, 2023, **27**, 101352, DOI: **10.1016/j.mtchem.2022.101352**.

61 C. D. Brites, P. P. Lima, N. J. Silva, A. Millán, V. S. Amaral, F. Palacio and L. D. Carlos, Thermometry at the nanoscale, *Nanoscale*, 2012, **4**, 4799–4829.

62 J. Drabik, R. Lisiecki and L. Marciniak, Optimization of the thermometric performance of single band ratiometric luminescent thermometer based on Tb^{3+} luminescence by the enhancement of thermal quenching of GSA-excited luminescence in TZPN glass, *J. Alloys Compd.*, 2021, **858**, 157690, DOI: **10.1016/j.jallcom.2020.157690**.

63 H. Lv, L. Luo, W. Li and P. Du, Manipulating Upconversion Emission and Thermochromic Properties of Ho^{3+}/Yb^{3+}-Codoped $Al_2Mo_3O_{12}$ Microparticles by Negative Lattice Expansion for Multimode Visual Optical Thermometry, *Inorg. Chem.*, 2022, **61**, 11442–11453, DOI: **10.1021/acs.inorgchem.2c01813**.

64 K. Saidi, M. Dammak, K. Soler-Carracedo and I. R. Martín, A novel optical thermometry strategy based on emission of Tm^{3+}/Yb^{3+} codoped $Na_3GdV_2O_8$ phosphors, *Dalton Trans.*, 2022, **51**, 5108–5117, DOI: **10.1039/D1DT03747A**.

65 X. Tian, J. Li, H. Sheng, T. Li, L. Guo, C. Ji, Z. Huang, J. Wen, X. Liu, C. Li, J. Li and Y. Peng, Luminescence and optical thermometry based on silico-carnotite $Ca_3Y_2Si_3O_{12}$:Pr^{3+} phosphor, *Ceram. Int.*, 2022, **48**, 3860–3868, DOI: **10.1016/j.ceramint.2021.10.171**.

66 Z. Liu and R. X. Wang, Luminescence thermometry based on downshifting and upconversion photoluminescence of $Bi_4Ti_3O_{12}$:Yb^{3+}/Pr^{3+} ceramic, *Chalcogenide Lett.*, 2022, **19**, 471, DOI: **10.15251/CL.2022.197.471**.

67 A. M. Kaczmarek, M. K. Kaczmarek and R. V. Deun, Er^{3+}-to-Yb^{3+} and Pr^{3+}-to-Yb^{3+} energy transfer for highly efficient near-infrared cryogenic optical temperature sensing, *Nanoscale*, 2019, **11**, 833–837, DOI: **10.1039/C8NR08348G**.

68 V. Kesarwani and V. K. Rai, Non-contact optical thermometry via non-thermally coupled levels in upconverting glass, *J. Appl. Phys.*, 2022, **132**, 113102, DOI: **10.1063/5.0109275**.

69 K. Saidi, M. Dammak, K. Soler-Carracedo and I. R. Martín, A Novel Optical Thermometry Strategy Based on Emission of Tm^{3+}/Yb^{3+} codoped $Na_3GdV_2O_8$ Phosphors, *Dalton Trans.*, 2022, **51**, 5108–5117, DOI: **10.1039/D1DT03747A**.